

Ruddlesden-Popper Phase Hybrid Halide Perovskite/ Small-Molecule Organic Blend Memory Transistor

Murali Gedda, Emre Yengel, Hendrik Faber, Fabian Paulus, Ming-Chun Tang, Zhang Siyuan, Prashant Kumar, Dipti R. Naphade, Yana Vaynzof, George Volonakis, Feliciano Giustino, and Thomas D. Anthopoulos**

Dr. M. Gedda, Dr. E. Yengel, Dr. H. Faber, Dr. M. C. Tang, Dr. P. Kumar, Dr. D. R. Naphade, Prof. T. D. Anthopoulos
King Abdullah University of Science and Technology (KAUST),
KAUST Solar Center (KSC),
Thuwal 23955-6900,
Saudi Arabia.
E-mail: thomas.anthopoulos@kaust.edu.sa; murali.gedda@kaust.edu.sa

Dr. F. Paulus, Prof. Y. Vaynzof
Integrated Centre for Applied Physics and Photonic Materials,
Centre for Advancing Electronics Dresden (CAED),
Technical University of Dresden,
Nöthnitzer Straße 61, 01187 Dresden,
Germany.

Dr. Z. Siyuan
Physical Measurement Laboratory,
National Institute of Standards and Technology (NIST),
Gaithersburg, Maryland 20899,
USA.

Dr. G. Volonakis,
Univ Rennes, ENSCR, INSA Rennes, CNRS, ISCR (Institut des Sciences Chimiques de Rennes), UMR 6226, Rennes F-35000, France

Prof. F. Giustino
Oden Institute for Computational Engineering and Sciences, The University of Texas at Austin, Austin, Texas 78712, USA
Department of Physics, The University of Texas at Austin, Austin, Texas 78712, USA
.

Keywords: 2D perovskite; additive engineering; perovskite-organic blends; non-volatile memory; floating-gate transistor

Abstract

Controlling the morphology of metal halide perovskite layers during processing is critical for the reliable manufacturing of optoelectronic devices. Here we report on a strategy to control the microstructure of solution-processed layered Ruddlesden-Popper phase perovskite films based on $(\text{PEA})_2\text{PbBr}_4$. The method relies on the addition of the organic semiconductor $\text{C}_8\text{-BTBT}$ directly into the perovskite formulation, where it facilitates the formation of large and near-single-crystalline quality platelet-like $(\text{PEA})_2\text{PbBr}_4$ domains overlaid by a 4-nm-thin $\text{C}_8\text{-BTBT}$ layer. Transistors based on $(\text{PEA})_2\text{PbBr}_4/\text{C}_8\text{-BTBT}$ channels exhibit unexpectedly large hysteresis window between forward and return gate bias sweeps. Material and device analysis combined with theoretical calculations suggest that the $\text{C}_8\text{-BTBT}$ -rich phase acts as the hole transporting channel, while the naturally forming quantum wells in the hybrid perovskite beneath act as the charge storage element where carriers from the channel can be injected, stored or extracted via tunneling. When tested as a non-volatile memory, the devices exhibit record memory window (>180 V), a high erase/write channel current ratio (10^4), good data retention and high endurance ($>10^4$ cycles). Our results highlight a new memory device concept for application in large-area electronics while highlighting a simple growth technique that could be exploited for the fabrication of various optoelectronic devices.

Main Text

Organic metal halide Ruddlesden–Popper phase perovskites are currently attracting increasing attention due to their superior chemical stability and resistance against humidity which makes them attractive for use in emerging optoelectronic applications including, solar cells, light-emitting diodes, field-effect transistors, resistive switches and memristors, to name but a few.^[1–3] To this end, different strategies have been explored to further improve the device performance and stability, including the synthesis of new materials, the use of innovative processing methodologies, and implementation of novel device architectures.^[4,5] Among these strategies, morphology engineering of the active perovskite layer has emerged as a promising route towards enhancing the film crystallinity and performance of the resulting devices.^[4–7]

Although in the field of photovoltaics the use of polycrystalline perovskite layers can still yield cells with high power conversion efficiency (PCE),^[8] the situation is markedly

different in thin-film transistors (TFTs) where the presence of grain boundaries has a detrimental effect in lateral charge transport.^[9–11] Thus for the development of reliable, high performance TFTs, the ability to simultaneously control the layer morphology and crystallinity becomes critical. In recent years, various approaches have been developed and implemented, including the use of additives, solvent and compositional engineering, thermal treatment, all the way to the incorporation of self-assembled monolayers (SAMs) for interface engineering.^[4–7] Among the various approaches reported, blending with an insulating polymer (i.e. composition engineering) has shown promise for controlling the perovskite layer morphology, albeit with limited success in terms of device performance due to the insulating nature of the polymer.^[12,13]

Motivated by these early studies but also from similar approaches exploited in the field of organic semiconductors,^[14–17] we investigated the possibility of controlling the crystallization kinetics of a layered hybrid perovskite by mixing it with a semiconducting organic small-molecule. In particular, we blended the 2D Ruddlesden–Popper phase perovskite (2D-RPP) phenethylammonium lead bromide ((PEA)₂PbBr₄) with the molecular organic semiconductor 2,7-dioctyl[1]benzothieno[3,2-b] benzothiophene (C₈-BTBT), and spin-coated the formulations at room temperature to form the solid layers (see *Experimental*). A pronounced effect on the morphology evolution of the resulting layer was observed and an optimal (PEA)₂PbBr₄:C₈-BTBT composition identified. Elemental analysis reveals that C₈-BTBT phase-separates vertically forming an ultrathin (≈ 4.2 nm) layer atop crystalline platelet-like (PEA)₂PbBr₄ domains, in a process closely resembling the vertical phase separation encountered in organic polymer/small-molecule blends.^[15–18] Using the hybrid bilayers as the channel results in transistors with extremely large, robust and temperature-independent operating hysteresis. Device analysis combined with theoretical calculations highlight the synergistic effects of hole transport along the C₈-BTBT-rich channel and quantum mechanical tunneling in and out the natural quantum well (QW) of the (PEA)₂PbBr₄ crystal beneath, as the origin of the hysteresis. These programmable device operating characteristics^[19] are exploited

to demonstrate robust non-volatile memory transistors that exhibit a large memory window (>180 V), high retention time (55,000 s), and high endurance (10,000 cycles) while maintaining a large current on/off ratio (10^4).

The $(\text{PEA})_2\text{PbBr}_4$ and $\text{C}_8\text{-BTBT}$ (**Figure 1a**) solutions were prepared separately and mixed at a later stage to form the various blend formulations (see *Experimental*). Three different perovskite/small-molecule volume ratios (vol%) were studied: 90/10 vol% (Blend-I), 75/25 vol% (Blend-II), and 50/50 vol% (Blend-III). All formulations were processed via spin-coating at room temperature inside a nitrogen-filled glovebox followed by thermal annealing (see *Experimental*). Polarized-light optical microscopy (POM) images of the formed layers are shown in **Figure S1** (*Supporting Information*). With the exception of Blend-II, all other layers appear heterogeneous and exhibit no electrical functionality, which will be discussed later. Interestingly, Blend-II formulation undergoes a clear and abrupt change during deposition yielding layers composed of large platelet-like domains. The topography of Blend-II layers and was further investigated using atomic force microscopy (AFM) and compared to the pristine $(\text{PEA})_2\text{PbBr}_4$ layer (**Figure 1b-c**). The neat $(\text{PEA})_2\text{PbBr}_4$ layer appears polycrystalline and rough with an average thickness of ≈ 500 nm as compared to ≈ 230 nm for the Blend-II layer (**Figure 1b-c** and **Figure S2**) with the latter appearing significantly more homogeneous featuring large, percolating, platelet-like domains 20-50 μm in size (**Figure 1c**). Analysis of the AFM height histograms in **Figure S2b** reveals a distinct bimodal distribution indicative of the existence of two plateaus, one at ≈ 112 nm (Plateau-1) and a second (Plateau-2) at ≈ 263 nm.

We further investigated the crystallinity of the formed layers using X-ray diffraction (XRD) measurements. **Figure 1d** shows the diffractograms for the neat $(\text{PEA})_2\text{PbBr}_4$ and Blend-II layers, while **Figure S3** displays the diffractograms for all four samples. The evenly spaced sharp diffraction peaks of (002) to (0010) confirms the formation of the 2D-RPP perovskite phase with a preferential out-of-plane orientation in all samples. Analysis of the diffractograms in **Figure 1d** and **Figure S3** shows that Blend-II layers exhibit enhanced

diffraction intensities and reduced peak widths, highlighting the key role of C₈-BTBT in mediating the crystallization and growth of the (PEA)₂PbBr₄ domains without distorting the 2D-RPP phase. Analysis of the (002) peak using the Debye-Scherrer method^[20] reveals a significant increase in the crystallite size from ≈ 75 nm, for neat (PEA)₂PbBr₄, to ≈ 123 nm for Blend-II layers (**Table S1**). The significant enlargement in the crystalline domains is expected to benefit carrier transport due to the presence of fewer grain boundaries.^[21,22]

To probe the influence of C₈-BTBT on the perovskite orientation with respect to the substrate, we performed two-dimensional XRD (2D-XRD) measurements (**Figure 2a**). The resulting diffractograms for the neat C₈-BTBT films show a major reflection at 3.10° corresponding to (001) plane (see red dotted line in **Figure 2b**), in agreement with previous reports.^[23] The neat (PEA)₂PbBr₄ layer, on the other hand, exhibits partial Debye-Scherrer diffraction rings with intense broad spots, which indicate the presence of mixed 2D-RPP phases corresponding to the different number of octahedron layers in the (PEA)₂PbBr₄ (known as the *n*-number in 2D-RPP), with considerable randomness in their orientation with respect to the substrate (see schematic illustration in **Figure 2e**).^[24] The central reflections at $\theta = 0^\circ$ are attributed to the (002) planes of the 2D perovskite and the calculated layer spacing of ≈ 1.65 nm is in line with reports in the literature.^[25,26] By contrast, Blend-II layers (**Figure 2a**) exhibit well-separated in-plane and out-of-plane diffraction spots, which are indicative of the presence of a single-crystalline phase with $n = 1$.^[24] **Figure 2c-d** depicts the orientation of the domains in (PEA)₂PbBr₄ formed without and with C₈-BTBT, respectively, with respect to the substrate. Calculating the full width at half maximum (FWHM) of the higher-order (002) reflections for the neat perovskite and Blend-II films, reveals that the latter exhibits consistently lower values, indicating the presence of larger crystalline domains as compared to neat (PEA)₂PbBr₄ (**Figure S4**). On the basis of these results we conclude that although the crystal lattice of (PEA)₂PbBr₄ remains unaffected by the presence of C₈-BTBT, the size, crystallinity and preferred orientation of the (PEA)₂PbBr₄ domains increases significantly.

Next, we studied the elemental composition and distribution in Blend-II layers using X-ray energy dispersive spectroscopy (EDS) (**Figure 3a**). The elemental maps for C, S, and Br indicate the homogeneous distribution of the elements within individual platelet-like islands. Although the same is valid for C and S outside the crystalline domains, this is not the case for Br as it is found primarily in regions corresponding to the crystalline platelet-like $(\text{PEA})_2\text{PbBr}_4$ domains. We thus conclude that $\text{C}_8\text{-BTBT}$ (C and S) is uniformly distributed across the entire layer, whereas $(\text{PEA})_2\text{PbBr}_4$ (Br) is primarily confined to the platelet-like domains of the composite layer. Additional information about the elemental composition of Blend-II layers was obtained via XPS measurements. **Figure 3b** shows the XPS spectra in the 195–135 eV range covering the Br 3p (195–175 eV), S 2p (165–160 eV), Si 2s (160–150 eV), and Pb 4f (150–135 eV) core levels. Even though the highest XPS intensity for Br and Si are the Br 3d (≈ 69 eV) and Si 2p (≈ 99 eV) core levels, showing all main elements in the same spectral range allows direct correlation of relative intensity ratio between Br, S, and Pb, with the specific probe depth without the need for elaborate calibrations. As can be seen in **Figure 3b**, the Pb 4f peaks are only observed in the neat $(\text{PEA})_2\text{PbBr}_4$ and the Blend-II layers, whereas the S 2p signature appears only in $\text{C}_8\text{-BTBT}$ and Blend-II layers confirming that the organic molecule and perovskite phase co-exist.

To probe the elemental composition in the vertical direction of Blend-II layers, we performed XPS depth profiling measurements using an Ar ion gun with ≈ 0.14 nm/s sputtering rate. Since the film fully etches at ≈ 1080 s, the thickness was estimated to be ≈ 150 nm. The bottom panel in **Figure 3b** shows the XPS spectra in the 195–135 eV spectral range after the initial three sputtering steps (up to 90 s). The S 2p peak disappears after the first 30 s of sputtering (≈ 4.2 nm), which implies that $\text{C}_8\text{-BTBT}$ is only distributed at the surface of the Blend-II layer. These results provide direct evidence for the presence of a vertically phase-separated $(\text{PEA})_2\text{PbBr}_4/\text{C}_8\text{-BTBT}$ system. **Figure 3c** shows a schematic illustration (not in scale) of the spontaneously formed bilayer system.

The charge transport characteristics in all three blend layers were evaluated in bottom-gate, top-contact (BG-TC) transistors and compared against those of neat (PEA)₂PbBr₄ TFTs (**Figure S5**). As already mentioned, transistors based on Blend-II (**Figure 4a**) are the only devices exhibiting *p*-channel behavior featuring prominent counter-clockwise hysteresis in the channel current (I_D) when sweeping the gate voltage (V_G) from positive (+100 V) to negative (-100 V) and back to positive potential. Despite the large hysteresis, Blend-II TFTs maintain a high channel current modulation of $>10^4$ with the operating characteristics remaining similar even after 100 repeated measuring cycles (**Figure 4b**), and when measured at different V_D (**Figure 4c**). These results suggest that in Blend-II transistors, hole accumulation occurs within the phase-separated C₈-BTBT-rich domain (≈ 4 nm-thick) atop the (PEA)₂PbBr₄ crystalline platelets. Altering the concentration of C₈-BTBT in the blend leads to polycrystalline layers and non-functioning transistors (**Figure S5**). For this reason, TFTs based on Blend-I and Blend-III were not considered any further here.

The origin of operating hysteresis in TFTs can be broadly attributed to three main processes: Dipole polarization (process-I), the presence of mobile ions (process-II), and charge trapping (process-III).^[27] Dipole switching (process-I) is commonly observed in memory transistors utilizing ferroelectric gate dielectrics.^[27] The process typically manifests as clockwise hysteresis (*p*-channel devices), which is clearly not the case here and as such it can be excluded (**Figure 4a-c**)^[19]. Process-II, on the other hand, is known to induce counter-clockwise hysteresis which is qualitative similar to that observed in **Figure 4a** and is frequently encountered in semiconductors containing mobile ions, including metal halide perovskites.^[28–30] In devices where process-II dominates, the hysteresis often depends on both the scan rate (V/s) of V_G during measurements, due to the field-driven displacement of mobile ions, and the sample temperature (T), since at low temperatures mobile ions freeze out. To test these hypotheses, we recorded the transfer characteristics for Blend-II transistor at different V_G scan rates from 1 to 5 V/s (**Figure 4d**) and at temperatures in the range 5–300 K (**Figure 4e**).

Evidently, no systematic dependence of hysteresis on either measurement parameter is observed. The only noticeable change is the small shift in the turn-on voltage (V_{ON}) in the forward scans with lowering T , an effect most likely attributed to the dependence of V_{ON} on T , often observed in organic TFTs.^[31,32] On the basis of these results, we conclude that mobile ion migration cannot explain the hysteresis observed in (PEA)₂PbBr₄/C₈-BTBT transistors (**Figure 4a**). Charge trapping (process-III) is the only remaining process that could account for hysteretic behaviour observed. Indeed, the presence of trap states in the channel of a p -type TFT is known to give rise to counter-clockwise hysteresis.^[27] However, the latter is often accompanied by strong temperature dependence characteristics, which is not observed here (**Figure 4e**).

Next, we studied the influence of the applied gate field on the device hysteresis by recording the transfer curves at V_G sweeping ranges of ± 25 , ± 30 , ± 50 , ± 75 and ± 100 V at a constant $V_D = -10$ V (**Figure 4f**). What becomes evident from these measurements is that a minimum V_G bias of ± 25 V is required for I_D to reach its maximum/minimum values (ON/OFF currents, respectively), suggesting that the gate field plays a key role in the hysteresis. Such a robust, temperature-independent and vertical electric-field dependent channel conductance behavior points to the presence of a “floating-gate” like system where charge trapping/de-trapping occurs via quantum mechanical tunneling - a temperature-independent process.^[33–35] By considering the phase-separated channel in **Figure 5a**, we hypothesize that the natural QW formed within the (PEA)₂PbBr₄ domain beneath the C₈-BTBT phase may act as the floating-gate able to capture holes in the presence of an electric field. Under charge accumulation conditions (ON state), holes start being injected from the conjugated core of BTBT across the C₈/PEA spacers (≈ 1.3 nm distance) to the PbBr₄ QW beneath via electric-field-assisted tunneling (**Figure 5b**) in a process described previously for layered hybrid perovskites.^[36] The ability of the layered hybrid perovskites to suppresses ion-migration^[37] may also explain the absence of ionic displacement in the temperature dependent measurements of **Figure 4e**.

In an effort to quantitatively describe the energy level alignment between C₈-BTBT and (PEA)₂PbBr₄, which is needed to support the quantum confinement and tunneling effects, we employed density functional theory (DFT) based calculations, using the Heyd–Scuseria–Ernzerhof (HSE) hybrid functional (see *Supporting Information*).^[38] **Figure S6a** shows the calculated energy level alignment of (PEA)₂PbBr₄ and the molecular crystal of C₈-BTBT based on the density-of-states calculations shown in **Figure S6b**. The energy levels of the two systems are aligned with respect to each other, using the measured valence band top of -6.30 eV^[39] and -5.05 eV^[40] for (PEA)₂PbBr₄ and C₈-BTBT, respectively. The resulting energy band diagram (**Figure S6a**) corresponds to a type-II band alignment between PbBr₄ and BTBT, and type-I between PEA and PbBr₄ that forms the QW where PEA is the barrier layer. This is not surprising since 2D-perovskites are known to act as naturally occurring QW systems.^[36,41] Based on the calculated density of states, C₈-BTBT can be also considered as a QW with the C₈ alkyl side chain confining the semiconducting back-bone (**Figure S6b**). The calculated lengths of the confinement layers are 10 and 16 Å for (PEA)₂PbBr₄ and C₈-BTBT, respectively. Overall, both energy band alignment and length of confinement support the injection/extraction of carriers in the perovskite QW through quantum mechanical tunneling across the organic spacers (potential barriers) form the C₈-BTBT channel, and at the same time explain the temperature-independent hysteresis observed (**Figure 4e**).

Having demonstrated the ability to reliably modulate the conductance state of the (PEA)₂PbBr₄/C₈-BTBT channel via the V_G field, we explored the use of Blend-II transistor as a non-volatile memory device. **Figure 5c** shows the transfer characteristic of a representative device and the V_G bias chosen to write, read and erase the conductance state of the channel, which represents the bit of data stored, i.e., ON state, and OFF state. **Figure S7a** shows the device energy band diagram, reconstructed using the calculated energetics from **Figure S6a**, while **Figure S7b-d** depicts the energy diagram at different biasing conditions [i.e., V_G = 0 V (read), forward sweep V_G, (write) and return sweep V_G (erase)]. As already discussed, the key

to the hysteretic behavior of these devices is the polarity and magnitude of V_G since it determines the probability of carrier tunneling from BTBT to the PbBr₄ QW across the ≈ 1.3 nm-thick organic spacers (**Figure 5b**). The presence, or absence, of holes into the QW affects the electrostatic potential landscape across the channel, ultimately determining the channel conductivity.

As shown in **Figure S7b**, prior to any V_G application, the octahedral PbBr₄ floating gate (i.e., the natural QW) is assumed neutral (no trapped charge). When the V_G becomes more negative with respect to the ground potential (source) (**Figure S7c**), holes start to accumulate in the BTBT phase while simultaneously being injected into the PbBr₄ QW via Fowler–Nordheim tunneling.^[42] Under this biasing condition, the channel current reaches a maximum value of $\approx 10^{-5}$ A (ON-current) at $V_G = -100$ V (**Figure 5c**). Removing the V_G bias results in holes being confined inside the QW, unable to escape due to the presence of the insulating barrier layers on either side (**Figure 4b**, **Figure S6a**). The bit of data stored can then be readout by measuring the device current at $V_G = 0$ V (“read” potential in **Figure 5c**). When a less negative V_G is applied (**Figure S7d**), the concentration of holes in the C₈-BTBT channel quickly diminishes, while holes confined in the PbBr₄ QW are simultaneously pumped back (i.e. de-trapped) to the C₈-BTBT channel via the same tunneling process. As the holes become fully depleted, the channel current reaches its lowest value of $\approx 3 \times 10^{-9}$ A (OFF-current) (**Figure 5c**) and it remains low until biasing with a more positive voltage (+100 V).

The large hysteresis window (ΔV_M) that envelopes the two conduction states remains unchanged during repeated measurements and exceeds 180 V (**Figure S8**). The latter value is higher than any ΔV_M reported previously for organic TFT-based memory device. However, we note that considering the magnitude of ΔV_M alone without taking into account the V_G range employed, would be misleading. In an effort to objectively compare our data with results from the literature, we calculated the ratio of ΔV_M with the operating voltage range (V_{OP}) applied at the gate terminal (i.e., $\Delta V_M/V_{OP}$). The calculated values, together with those extracted from the

literature, are summarized in **Table S2**. Evidently, the (PEA)₂PbBr₄/C₈-BTBT transistors yield a $\Delta V_M/V_{OP}$ of ≈ 0.9 , which is the highest reported value to date for organic TFTs.^[43–52]

To evaluate the suitability of Blend-II transistors as a practical non-volatile memory device, we studied the endurance and data retention characteristics at room temperature. **Figure 5d** displays the endurance results for a device subjected to 10,000 repeated programming cycles (write, read and erase steps) using the gate voltage waveform shown in the inset. The channel current in both ON and OFF states remain almost unaltered, highlighting a robust device operation. Next, we investigated the ability of Blend-II transistors to retain the programmed data as a function of time; the so-called data retention time. For the purpose of this experiment, a single writing (or erasing) voltage pulse was applied to the gate terminal, followed by sequential reading steps at predefined time intervals over a period of 55,000 s. **Figure 5e** illustrates the evolution of both the ON and OFF currents across the device as a function of time following the application of the programming step i.e., write or erase (see inset in **Figure 5e**). Evidently, the device is able to retain the pre-programmed ON or OFF state over the entire testing period, suggesting a much longer intrinsic data retention time. Lastly, we evaluate the memory performance as a function of programming (writing/erasing) speed. As shown in **Figure 5f**, even the shortest pulse of 200 ms is sufficient to program the ON and OFF states in the device, with only a small decrease observed in the ON current for the shortest pulse width. Although scaling-down the channel length is anticipated to lead to faster programming times, the achieved speed is already adequate for a variety of low-end applications and is comparable with previously reported values for organic-based memories TFTs (**Table S2**).

To summarize, we have reported on a new strategy to grow highly crystalline hybrid perovskite/small-molecule bilayers via one-step solution processing. The organic molecule was shown to play a key role in controlling the crystallization and growth of the 2D-RPP perovskite phase, leading to the spontaneous formation of platelet like domains with near single-crystalline quality overlaid by a ≈ 4.2 nm-thin small-molecule layer. Transistors made with the hybrid

bilayer as the channel exhibited surprisingly large operating hysteresis, a property related to synergistic hole transport across the small-molecule phase atop and the simultaneous field-driven carrier de/trapping from the natural quantum well in the perovskite beneath. When tested as non-volatile memory device, the transistor showed a large memory window of 180 V with a $\Delta V_M/V_{OP}$ ratio of 0.9; the highest reported to date for organic TFT memory devices (**Table S2**). The exceptional endurance demonstrated combined with promising data retention and the high current ON/OFF ratio achieved, makes the proposed memory transistor concept promising for application in large-area electronics. Lastly, we anticipate our approach to control the microstructure of hybrid perovskites may find use in different device applications including light-emitting diodes, solar cells and photodetectors, to name but a few.

Experimental

Material Preparation: The $(PEA)_2PbBr_4$ precursor solution of 0.2 M concentration was prepared by dissolving 1:2 molar ratio of $PbBr_2$ and $C_6H_5C_2H_4NH_3Br$ (PEABr) in dimethylformamide (DMF) while heated at 75 °C and under dynamic mixing for 5 h. The C₈-BTBT solution of 0.02 M was prepared separately using chlorobenzene (CB) as the solvent. The blend precursor formulations were prepared with three different perovskite/organic volume ratios (vol%) of: 90/10 (Blend-I), 75/25 (Blend-II) and 50/50 (Blend-III).

Transistor fabrication and characterization: The transistors in a back gate – top contact (BG-TC) architecture were fabricated on heavily doped Si (Si^{++}) wafers with 300 nm thermally grown SiO_2 , acting as the gate electrode and gate dielectric, respectively. Before thin-film deposition, the Si^{++}/SiO_2 wafers were thoroughly cleaned using a series of ultra-sonication baths of de-ionized (DI) water, acetone and 2-propanol for 10 min each, followed by a UV-ozone treatment step for 15 min. The pre-prepared formulations were filtered and spun on Si^{++}/SiO_2 substrates, followed by thermal annealing at 70 °C for 5 min in the dry nitrogen atmosphere.

Transistor fabrication was completed by the thermal deposition of a top Au source and drain electrodes under a high vacuum ($\sim 1 \times 10^{-6}$ mbar). The channel width (W) and length (L) of the resulting devices were 1000 μm and 40 μm , respectively. The electrical current-voltage characterization of the transistors at room temperature was carried out in a nitrogen glove box using a precision source/measure unit, B2912A (Keysight Technologies). A home-built MATLAB script has been employed to probe various characteristics of a memristor.

X-ray Diffraction Measurements: Bruker D8 ADVANCE diffractometer with a monochromatic Cu - K_{α} radiation beam with wavelength $\lambda = 0.154$ nm was used for X-ray diffraction measurements. The thin-films were studied in powder diffraction mode using θ - 2θ scan configuration to detect crystallites with a reciprocal lattice vector perpendicular to the film surface.

Atomic Force Microscopy: The surface topography information for all the samples was measured via intermittent contact mode AFM using a ND-MDT SOLVAR NEXT scanning probe microscope in the air at room temperature. The measurements were performed using Pt/Ir coated Si tips of resonance frequency ranging between 150-300 Hz.

SEM imaging and EDX Mapping: Zeiss MERLIN Field Emission Scanning Electron Microscope (FESEM) with OXFORD EDS was used to characterize the surface morphology of obtained material and elemental mapping. X-ray energy of 25 kV was maintained while scanning the samples.

2D X-ray Diffraction: The XRD measurements of the organic, perovskite and blend films were conducted on a Rigaku SmartLab diffractometer equipped with a 9 kW rotating copper anode. The 2D diffraction maps were recorded using a 2D HyPix3000 detector in a coupled $\theta - 2\theta$ scan (beam collimator 0.2 mm ϕ) at a detector distance of 110 mm. The direct beam was blanked with a beam blanker. Data processing, optics and sample alignment, and measurements

were performed using the Rigaku SmartLab Guidance and 2DP software. The maps were background corrected. 1D profiles were obtained by integrating a central slice of the corrected 2D map, representing a standard Bragg-Brentano scan. Intensities (log scale) were normalized to account for variations in film thickness and contributions from the $k\beta$ line were stripped.

XPS Depth Profiling: Kratos Axis UltraDLD XPS/UPS system, using the monochromatic Al $k\alpha$ line, is used to acquire XPS spectra. The base pressure of the analysis chamber is 10^{-8} Torr. The spectra were calibrated with the C—C bond in C 1s peak, and set to BE = 284.5 eV. All samples were characterized at a normal take-off angle unless stated otherwise. The Fermi level was calibrated using atomically clean gold and the presented spectra were calibrated versus the Fermi level at zero binding energy. XPS depth profiling is done by using an Ar-ion gun with power 1 kV and 600 nA on a raster area of 1 mm².

Supporting Information

Supporting Information is available from the Wiley Online Library or from the author.

Acknowledgments

This publication is based upon work supported by the King Abdullah University of Science and Technology (KAUST) Office of Sponsored Research (OSR) under Award No: OSR-2016-CRG5-3029

Received: ((will be filled in by the editorial staff))

Revised: ((will be filled in by the editorial staff))

Published online: ((will be filled in by the editorial staff))

References

- [1] Z. Chen, Y. Guo, E. Wertz, J. Shi, *Adv. Mater.* **2019**, *31*, 1803514.
- [2] J. Hu, L. Yan, W. You, *Adv. Mater.* **2018**, *30*, 1802041.
- [3] Y. Lin, P. Pattanasattayavong, T. D. Anthopoulos, *Adv. Mater.* **2017**, *29*, 1702838.
- [4] C.-Y. Chang, C.-Y. Chu, Y.-C. Huang, C.-W. Huang, S.-Y. Chang, C.-A. Chen, C.-Y. Chao, W.-F. Su, *ACS Appl. Mater. Interfaces* **2015**, *7*, 4955.

- [5] Y. Li, L. Ji, R. Liu, C. Zhang, C. H. Mak, X. Zou, H.-H. Shen, S.-Y. Leu, H.-Y. Hsu, *J. Mater. Chem. A* **2018**, *6*, 12842.
- [6] P. Cheng, Z. Xu, J. Li, Y. Liu, Y. Fan, L. Yu, D.-M. Smilgies, C. Müller, K. Zhao, S. F. Liu, *ACS Energy Lett.* **2018**, *3*, 1975.
- [7] X. Zhang, R. Munir, Z. Xu, Y. Liu, H. Tsai, W. Nie, J. Li, T. Niu, D.-M. Smilgies, M. G. Kanatzidis, A. D. Mohite, K. Zhao, A. Amassian, S. F. Liu, *Adv. Mater.* **2018**, *30*, 1707166.
- [8] L. Gao, G. Yang, *Sol. RRL* **2019**, *4*, 1900200.
- [9] J. Qiu, Y. Zheng, Y. Xia, L. Chao, Y. Chen, W. Huang, *Adv. Funct. Mater.* **2019**, *29*, 1806831.
- [10] P. K. Nayak, D. T. Moore, B. Wenger, S. Nayak, A. A. Haghighirad, A. Fineberg, N. K. Noel, O. G. Reid, G. Rumbles, P. Kukura, K. A. Vincent, H. J. Snaith, *Nat. Commun.* **2016**, *7*, 13303.
- [11] J. G. Labram, D. H. Fabini, E. E. Perry, A. J. Lehner, H. Wang, A. M. Glaudell, G. Wu, H. Evans, D. Buck, R. Cotta, L. Echegoyen, F. Wudl, R. Seshadri, M. L. Chabiny, *J. Phys. Chem. Lett.* **2015**, *6*, 3565.
- [12] T. H. Han, J. W. Lee, C. Choi, S. Tan, C. Lee, Y. Zhao, Z. Dai, N. De Marco, S. J. Lee, S. H. Bae, Y. Yuan, H. M. Lee, Y. Huang, Y. Yang, *Nat. Commun.* **2019**, *10*, 1.
- [13] A. Fakharuddin, M. Seybold, A. Agresti, S. Pescetelli, F. Matteocci, M. I. Haider, S. T. Birkhold, H. Hu, R. Giridharagopal, M. Sultan, I. Mora-Seró, A. Di Carlo, L. Schmidt-Mende, *ACS Appl. Mater. Interfaces* **2018**, *10*, 42542.
- [14] R. Hamilton, J. Smith, S. Ogier, M. Heeney, J. E. Anthony, I. McCulloch, J. Veres, D. D. C. Bradley, T. D. Anthopoulos, *Adv. Mater.* **2009**, *21*, 1166.
- [15] A. F. Paterson, L. Tsetseris, R. Li, A. Basu, H. Faber, A. H. Emwas, J. Panidi, Z. Fei, M. R. Niazi, D. H. Anjum, M. Heeney, T. D. Anthopoulos, *Adv. Mater.* **2019**, *31*, 1900871.

- [16] K. Zhao, O. Wodo, D. Ren, H. U. Khan, M. R. Niazi, H. Hu, M. Abdelsamie, R. Li, E. Q. Li, L. Yu, B. Yan, M. M. Payne, J. Smith, J. E. Anthony, T. D. Anthopoulos, S. T. Thoroddsen, B. Ganapathysubramanian, A. Amassian, *Adv. Funct. Mater.* **2016**, *26*, 1737.
- [17] J. Panidi, A. F. Paterson, D. Khim, Z. Fei, Y. Han, L. Tsetseris, G. Vourlias, P. A. Patsalas, M. Heeney, T. D. Anthopoulos, *Adv. Sci.* **2018**, *5*, 1700290.
- [18] R. Hamilton, J. Smith, S. Ogier, M. Heeney, J. E. Anthony, I. McCulloch, J. Veres, D. D. C. Bradley, T. D. Anthopoulos, *Adv. Mater.* **2009**, *21*, 1166.
- [19] M. Egginger, S. Bauer, R. Schwödiauer, H. Neugebauer, N. S. Sariciftci, *Monatshefte für Chemie* **2009**, *140*, 735.
- [20] A. R. Stokes, A. J. C. Wilson, *Math. Proc. Cambridge Philos. Soc.* **1942**, *38*, 313.
- [21] K. M. Boopathi, R. Mohan, T.-Y. Huang, W. Budiawan, M.-Y. Lin, C.-H. Lee, K.-C. Ho, C.-W. Chu, *J. Mater. Chem. A* **2016**, *4*, 1591.
- [22] B. A. Jones, A. Facchetti, M. R. Wasielewski, T. J. Marks, *Adv. Funct. Mater.* **2008**, *18*, 1329.
- [23] Y. Yuan, G. Giri, A. L. Ayzner, A. P. Zoombelt, S. C. B. Mannsfeld, J. Chen, D. Nordlund, M. F. Toney, J. Huang, Z. Bao, *Nat. Commun.* **2014**, *5*, 3005.
- [24] R. L. Milot, R. J. Sutton, G. E. Eperon, A. A. Haghighirad, J. Martinez Hardigree, L. Miranda, H. J. Snaith, M. B. Johnston, L. M. Herz, *Nano Lett.* **2016**, *16*, 7001.
- [25] D. Ma, Y. Fu, L. Dang, J. Zhai, I. A. Guzei, S. Jin, *Nano Res.* **2017**, *10*, 2117.
- [26] K. Shibuya, M. Koshimizu, F. Nishikido, H. Saito, S. Kishimoto, IUCr, *Acta Crystallogr. Sect. E Struct. Reports Online* **2009**, *65*, m1323.
- [27] V. Georgiou, D. Veksler, J. P. Campbell, P. R. Shrestha, J. T. Ryan, D. E. Ioannou, K. P. Cheung, *Adv. Funct. Mater.* **2018**, *28*, 1705250.
- [28] B. Hwang, J.-S. Lee, *Adv. Electron. Mater.* **2019**, *5*, 1800519.
- [29] S. P. Senanayak, B. Yang, T. H. Thomas, N. Giesbrecht, W. Huang, E. Gann, B. Nair,

- K. Goedel, S. Guha, X. Moya, C. R. McNeill, P. Docampo, A. Sadhanala, R. H. Friend, H. Sirringhaus, *Sci. Adv.* **2017**, *3*, e1601935.
- [30] M. H. Futscher, J. M. Lee, L. McGovern, L. A. Muscarella, T. Wang, M. I. Haider, A. Fakharuddin, L. Schmidt-Mende, B. Ehrler, *Mater. Horizons* **2019**, *6*, 1497.
- [31] M. Abbas, A. Pivrikas, E. Arici, N. Tekin, M. Ullah, H. Sitter, N. S. Sariciftci, *J. Phys. D Appl. Phys* **2013**, *46*, 495105.
- [32] Y. J. Lin, Y. C. Lin, *AIP Adv.* **2014**, *4*, 107105.
- [33] S. M. Sze, K. K. Ng, in *Phys. Semicond. Devices*, John Wiley & Sons, Inc., Hoboken, NJ, USA, **2006**, pp. 415–465.
- [34] C. Joachim, M. A. Ratner, *Proc. Natl. Acad. Sci. U. S. A.* **2005**, *102*, 8801.
- [35] H. C. Seong, B. S. Kim, C. D. Frisbie, *Science* **2008**, *320*, 1482.
- [36] B. Traore, L. Pedesseau, L. Assam, X. Che, J. C. Blancon, H. Tsai, W. Nie, C. C. Stoumpos, M. G. Kanatzidis, S. Tretiak, A. D. Mohite, J. Even, M. Kepenekian, C. Katan, *ACS Nano* **2018**, *12*, 3321.
- [37] Y. Lin, Y. Bai, Y. Fang, Q. Wang, Y. Deng, J. Huang, *ACS Energy Lett.* **2017**, *2*, 1571.
- [38] A. V. Krukau, O. A. Vydrov, A. F. Izmaylov, G. E. Scuseria, *J. Chem. Phys.* **2006**, *125*, 224106.
- [39] X. Yang, Z. Chu, J. Meng, Z. Yin, X. Zhang, J. Deng, J. You, *J. Phys. Chem. Lett.* **2019**, *10*, 2892.
- [40] A. F. Paterson, Y. H. Lin, A. D. Mottram, Z. Fei, M. R. Niazi, A. R. Kirmani, A. Amassian, O. Solomeshch, N. Tessler, M. Heeney, T. D. Anthopoulos, *Adv. Electron. Mater.* **2018**, *4*, 1700464.
- [41] M. Kepenekian, B. Traore, J. C. Blancon, L. Pedesseau, H. Tsai, W. Nie, C. C. Stoumpos, M. G. Kanatzidis, J. Even, A. D. Mohite, S. Tretiak, C. Katan, *Nano Lett.* **2018**, *18*, 5603.
- [42] M. Lenzlinger, E. H. Snow, *J. Appl. Phys.* **1969**, *40*, 278.

- [43] Y. Wang, Y. Yang, P. Ding, Q. Wei, X. Gao, S. Wang, C. Liu, A. Li, J. Yin, Y. Xia, Z. Liu, *Adv. Electron. Mater.* **2019**, *5*, 1800865.
- [44] S. J. Kim, J. S. Lee, *Nano Lett.* **2010**, *10*, 2884.
- [45] Y. H. Chou, S. Takasugi, R. Goseki, T. Ishizone, W. C. Chen, *Polym. Chem.* **2014**, *5*, 1063.
- [46] W. Li, F. Guo, H. Ling, P. Zhang, M. Yi, L. Wang, D. Wu, L. Xie, W. Huang, *Adv. Sci.* **2017**, *4*, 1700007.
- [47] H. C. Chang, C. L. Liu, W. C. Chen, *Adv. Funct. Mater.* **2013**, *23*, 4960.
- [48] Y. Park, K. J. Baeg, C. Kim, *ACS Appl. Mater. Interfaces* **2019**, *11*, 8327.
- [49] K. J. Baeg, Y. Y. Noh, H. Sirringhaus, D. Y. Kim, *Adv. Funct. Mater.* **2010**, *20*, 224.
- [50] Z. H. Wu, W. J. Sun, H. H. Tian, Z. F. Yu, R. X. Guo, X. Shao, H. L. Zhang, *Adv. Electron. Mater.* **2019**, *5*, 1800598.
- [51] L. A. Frolova, A. A. Rezvanova, V. Z. Shirinian, A. G. Lvov, A. V. Kulikov, M. M. Krayushkin, P. A. Troshin, *Adv. Electron. Mater.* **2016**, *2*, 1500219.
- [52] L. Song, Y. Wang, Q. Gao, Y. Guo, Q. Wang, J. Qian, S. Jiang, B. Wu, X. Wang, Y. Shi, Y. Zheng, Y. Li, *ACS Appl. Mater. Interfaces* **2017**, *9*, 18127.
- [53] K. Z. Du, Q. Tu, X. Zhang, Q. Han, J. Liu, S. Zauscher, D. B. Mitzi, *Inorg. Chem.* **2017**, *56*, 9291.
- [54] S. J. Kim, J. S. Lee, *Nano Lett.* **2010**, *10*, 2884.
- [55] W. Li, F. Guo, H. Ling, P. Zhang, M. Yi, L. Wang, D. Wu, L. Xie, W. Huang, *Adv. Sci.* **2017**, *4*, 1700007.

Figures

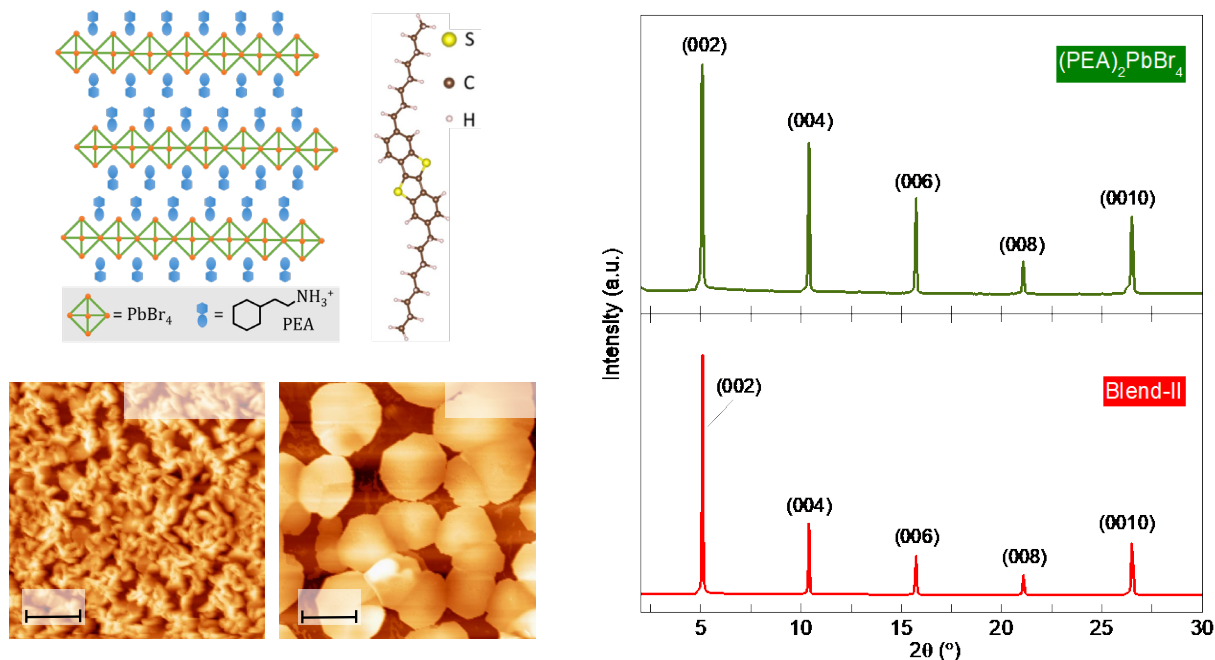


Figure 1. (a) Illustration of the 2D layered perovskite $(\text{PEA})_2\text{PbBr}_4$ and organic small-molecule $\text{C}_8\text{-BTBT}$. Atomic force microscopy images of pristine $(\text{PEA})_2\text{PbBr}_4$ (b), and Blend-II (c) layers. (d) Out-of-plane XRD patterns measured for $(\text{PEA})_2\text{PbBr}_4$ and Blend-II films.

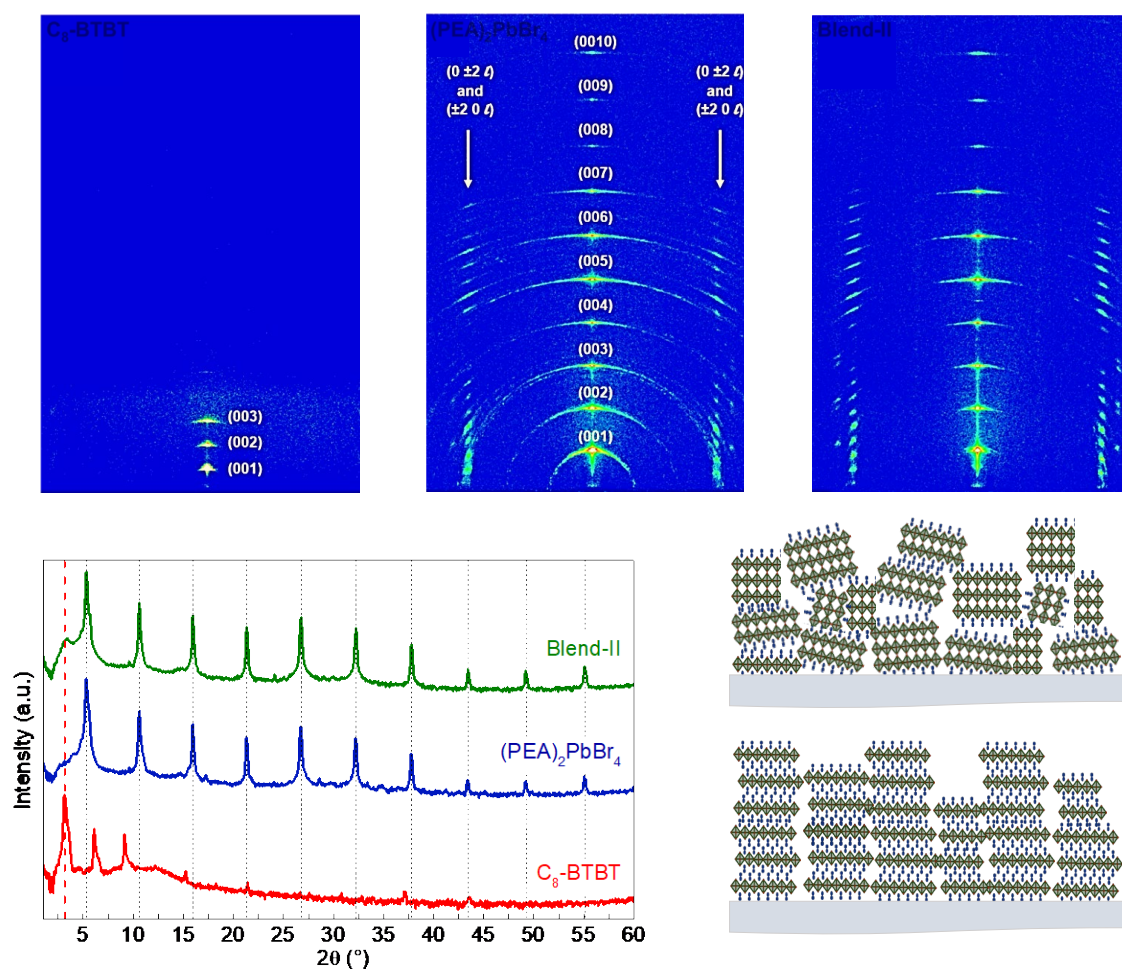


Figure 2. 2D-XRD diffraction pattern of coupled $\theta/2\theta$ scans measured for (a) spin-coated C₈-BTBT, pristine (PEA)₂PbBr₄, and Blend-II. (b) 1D diffraction pattern (central slice) with a logarithmic intensity scale. Schematic depiction of the orientation of the 2D-perovskite domains for pristine (PEA)₂PbBr₄ (c), and Blend-II (d) layers. In (d) the C₈-BTBT is not shown for simplicity.

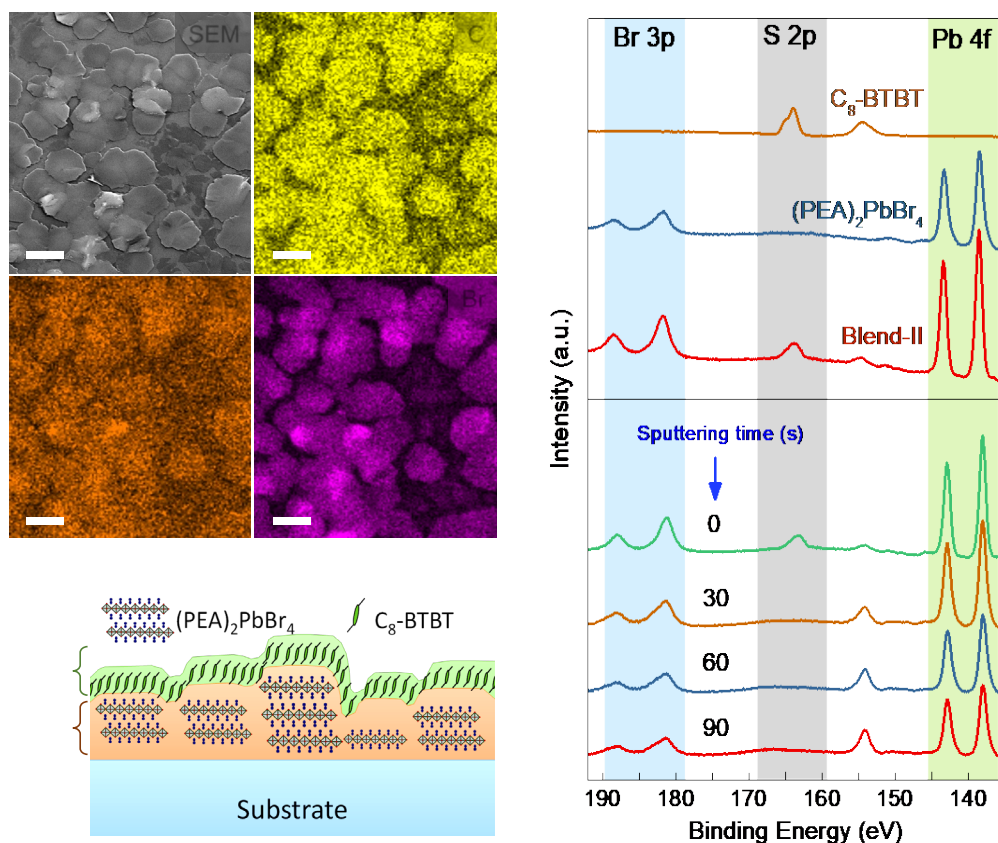


Figure 3. a) SEM-EDS elemental mapping of Carbon (C), Sulfur (S), Bromine (Br) and Lead (Pb). In all images, the scale bar is 20 μm. b) XPS survey scans of C₈-BTBT, (PEA)₂PbBr₄ and Blend-II (top frame) and depth profiling of Blend-II at different sputtering times (bottom frame). c) Schematic illustration of the vertically phase-separated Blend-II layer.

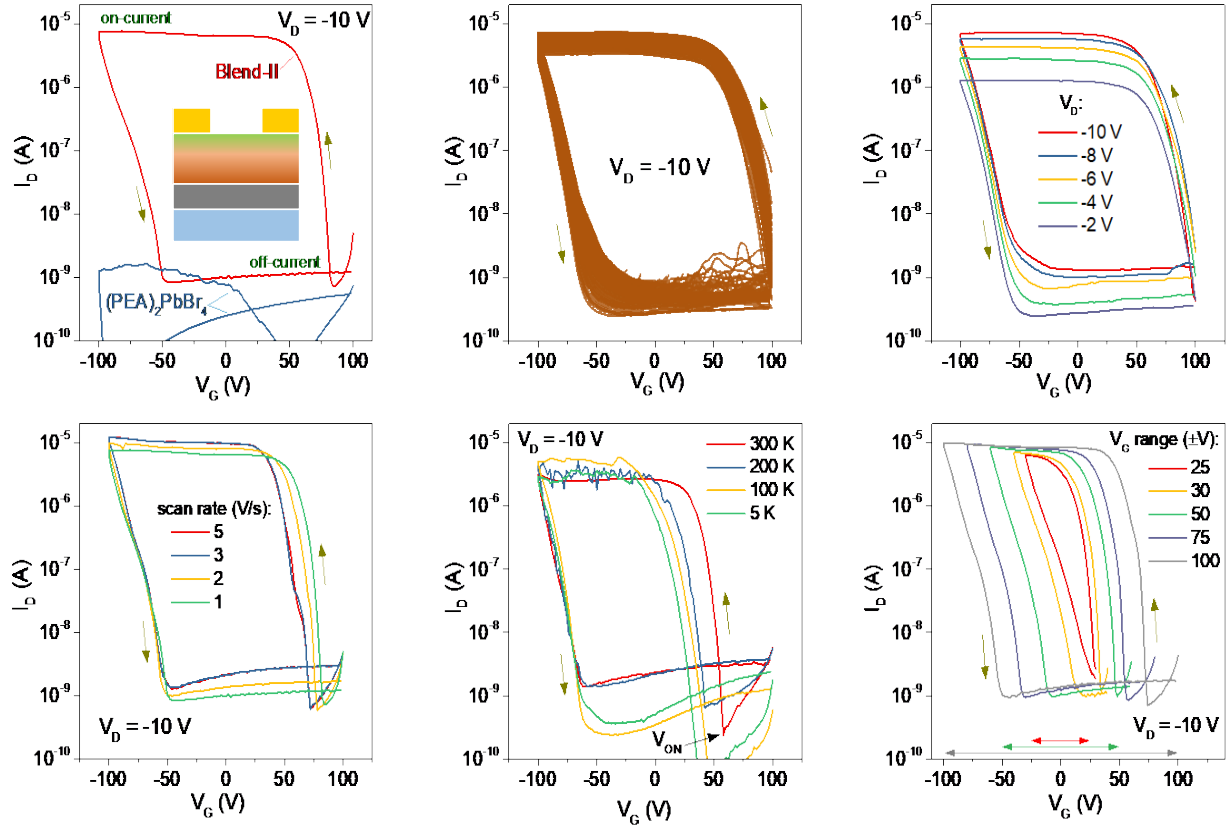


Figure 4. a) Charge transfer characteristics of $(\text{PEA})_2\text{PbBr}_4$ and Blend-II based FETs. Inset is the schematic of the device. b) Multiple hysteresis loops up to 100 continuous cycles. Device hysteresis behavior with c) drain voltage and d) scan rate. e) Temperature-dependent hysteresis behavior of the memristor. f) Variation in hysteresis window for different gate voltage scan ranges.

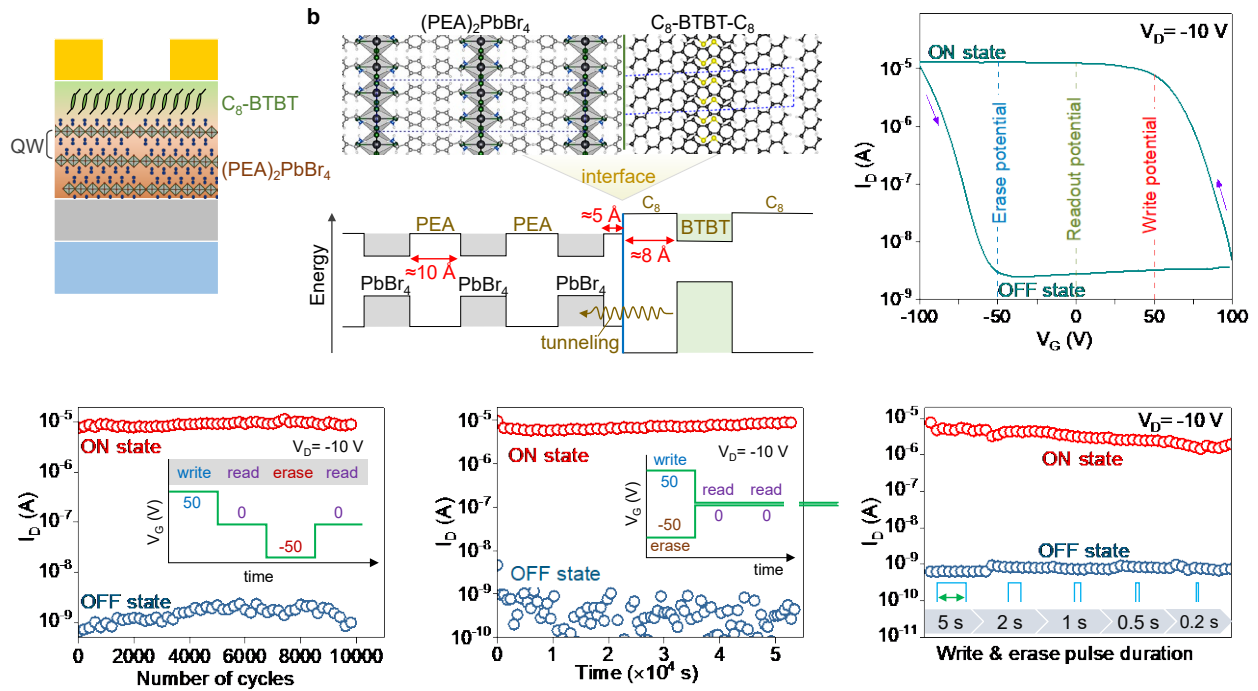


Figure 5. a) The schematic of a transistor incorporating the phase-separated Blend-II as the channel layer. b) Schematic of the energy level alignment between the organic and inorganic counterparts of (PEA)₂PbBr₄ and C₈-BTBT. c) Representative transistor transfer curve depicting the programming/reading/erasing potentials used for device testing. d) Endurance performance of the memristor subjected to 10,000 continuous ON-OFF programming cycles. e) Memory retention characteristics monitored for 55,000 s. f) Memory switching behavior using different write/erase pulse width ranging from 5 to 0.2 s.

Supporting Information

Ruddlesden-Popper Phase Hybrid Halide Perovskite/ Small-Molecule Organic Blend Memory Transistor

*Murali Gedda, Emre Yengel, Hendrik Faber, Fabian Paulus, Ming-Chun Tang, Zhang Siyuan, Prashant Kumar, Dipti R. Naphade, Yana Vaynzof, George Volonakis, Feliciano Giustino, Thomas D. Anthopoulos**

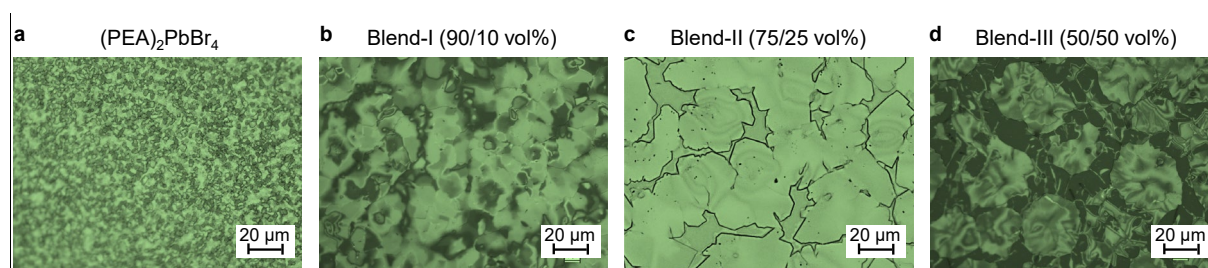


Figure S1. Optical micrographs of a) $(\text{PEA})_2\text{PbBr}_4$, b) Blend-I, c) Blend-II and d) Blend-III perovskite films.

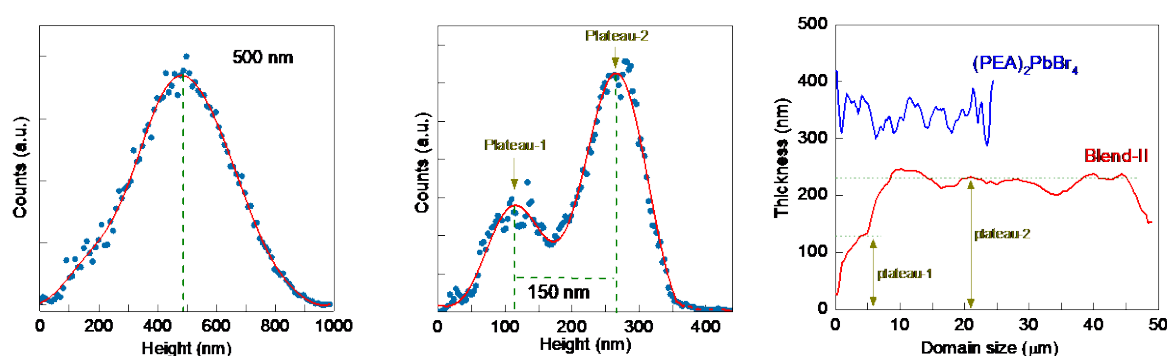


Figure S2. Height histograms extracted from AFM topographic images shown in **Figure 1** for the neat $(\text{PEA})_2\text{PbBr}_4$ (a), and Blend-II (b), layers. (c) Radial average profiles extracted from the same AFM images for the neat $(\text{PEA})_2\text{PbBr}_4$ and Blend-II layers.

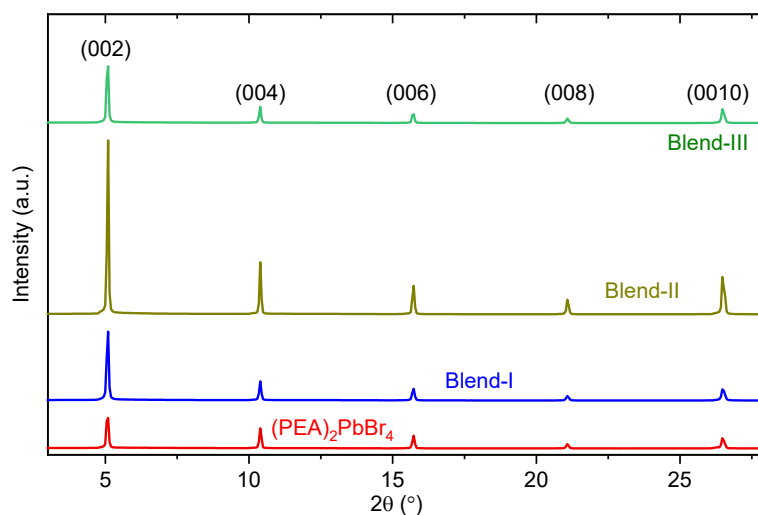


Figure S3. XRD patterns measured for neat and all three blend perovskite films.

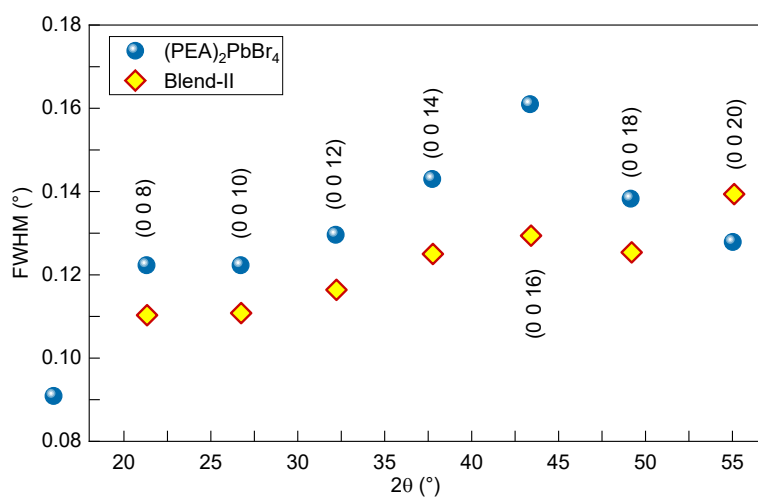


Figure S4. Comparison of the FWHM for higher-order (0 0 *l*) reflections after fitting Pseudo Voigt functions. The Blend always exhibits sharper reflections indicating the presence of larger crystallites.

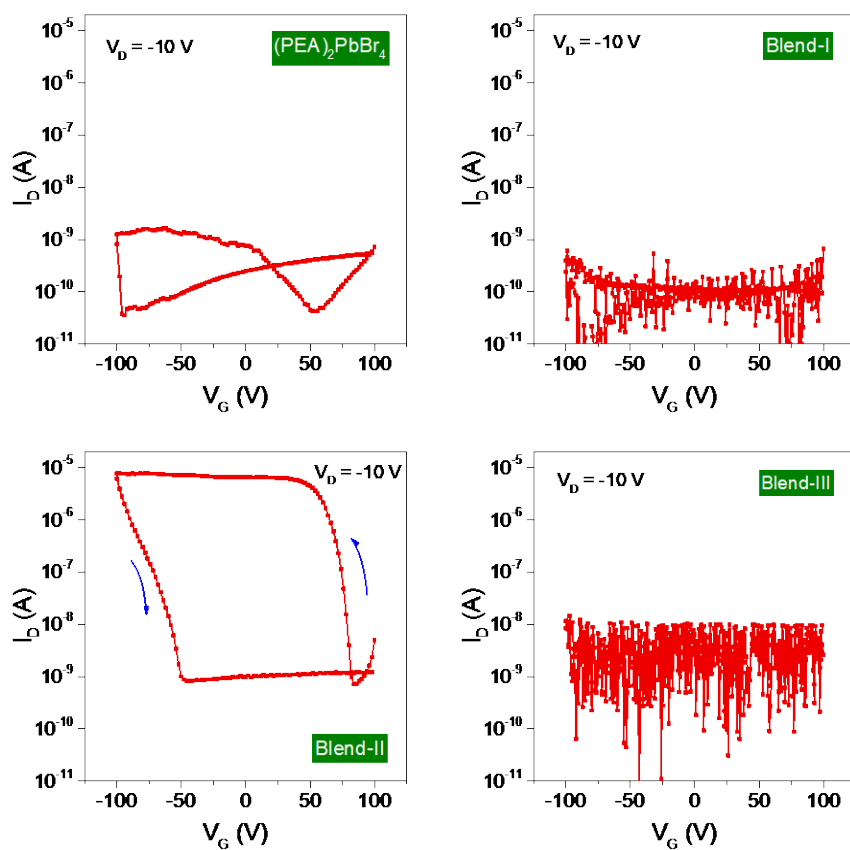


Figure S5. Transfer characteristics at fixed drain bias -10 V of a) $(\text{PEA})_2\text{PbBr}_4$, b) Blend-I, c) Blend-II and d) Blend-III perovskites based FETs.

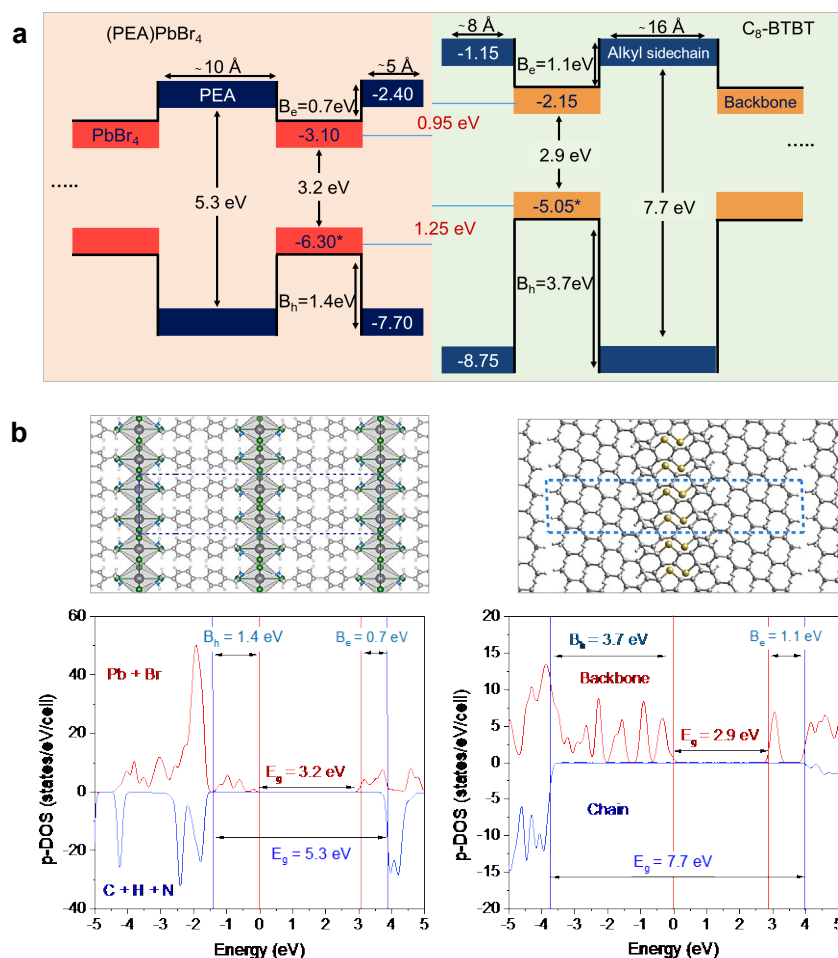


Figure S6. Energy level alignment between C₈-BTBT and (PEA)₂PbBr₄ (a), constructed using the atomistic model and projected density-of-states within DFT-HSE hybrid functional for the inorganic (red) and organic (blue) part of (PEA)₂PbBr₄ and C₈-BTBT (b). The blue dashed line on the atomistic models of (PEA)₂PbBr₄ and C₈-BTBT shows the lattice unit-cell.

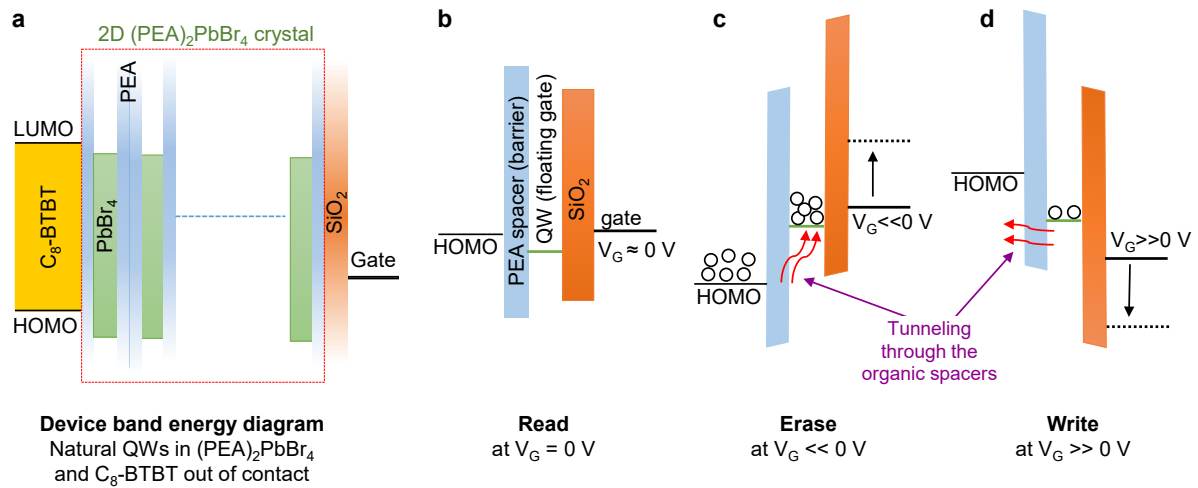


Figure S7. a) Simplified energy band diagram of the Blend-II based floating gate transistor. Energy band diagrams of the same device under different operational modes: (b) read, (c) write, and (d) erase bias conditions. Open circles represent hole charge carriers.

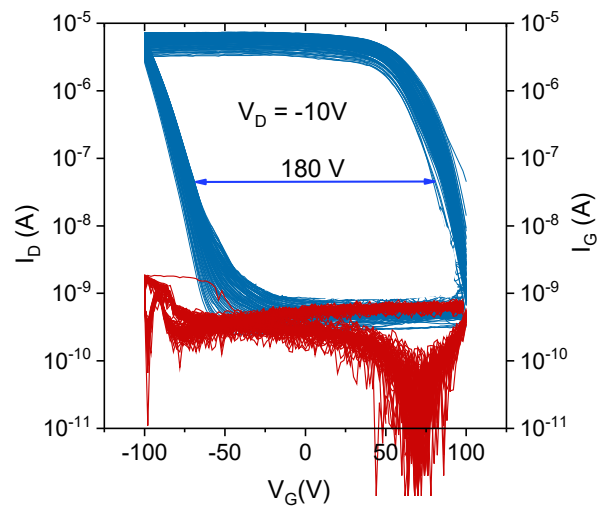


Figure S8. Hysteresis loops for 100 continuous repetitions of Blend-II based transistor.

Theoretical calculation

Calculations have been performed using the experimental structure of (PEA)₂PbBr₄, which is deposited in the Cambridge Structure Database (1542460) and Ref. Du *et al.*^[53] The lattice is orthorhombic with lattice parameters of $a = 33.35$ Å, $b = 8.146$ Å, $c = 8.123$ Å. The atomistic

model is shown in Figure S6. The structure is a two-dimensional halide perovskite, with $n=1$, and the spacer is the organic PEA ($\text{NH}_2\text{-CH}_2\text{-Ph}$). The unit cell has two layers of PbBr_4 octahedra, which results in a total of 164 atoms. We perform calculations without optimizing the structure (fixed atoms + cell) employing the HSE hybrid functional. We calculate the projected density-of-states (p-DOS) that is shown in Figure S6a. Blues are the contributions of the organic part (C, N, H atoms) and red shows the inorganic part (Pb+Br). The bandgap (E_g) of the compound is found at 3.2 eV, and the valence band top and bottom are comprised of Pb and Br, as expected. The first occupied states that belong to the organic parts are found at 1.4 eV below the valence band top, and the first unoccupied states at 0.7 eV above the conduction bands. The total bandgap for the organic part of perovskite obtained as 5.3 eV. Figure S8a shows the final confinement picture. The size of the confinement is 10.7 Å for the wide-bandgap organic part, and 6 Å for the semiconducting inorganic sites. This level diagram corresponds to a type-I band alignment. Similar calculations are extended to the organic small molecule, $\text{C}_8\text{-BTBT}$ using the experimental structure from a reference.^[40] The bandgap (E_g) of the small molecule is found at 2.9 eV. The first occupied states that belong to the 1-octyl part of $\text{C}_8\text{-BTBT}$ are found at 3.7 eV below the valence band top, and the first unoccupied states at 1.1 eV above the conduction bands. The total bandgap for the 1-octyl side chain of small molecule estimated as 7.7 eV.

Table S1. Calculated crystallite sizes of $(\text{PEA})_2\text{PbBr}_4$ and Blend-II films using the Debye-Scherrer equation.

| Material | 2 θ (°) | FWHM (2 θ) | Crystallite size (nm) |
|-------------------------------|----------------|--------------------|-----------------------|
| $(\text{PEA})_2\text{PbBr}_4$ | 5.28 | 0.1113 | 74 |
| Blend -II | 5.28 | 0.0676 | 123 |

Table S2. Comparison of key operating parameters of Blend-II based transistors with organic-based TFT memory devices from the literature.

| Channel material | Dielectric material | Charge storage element | Operating voltage (V_{OP}) | Memory window ΔV_M (V) | $\frac{\Delta V_M}{V_{OP}}$ | Endurance cycles | Writing/erasing speed | Ref. |
|---------------------------------|--------------------------------|--------------------------------------|--------------------------------|--------------------------------|-----------------------------|------------------|-----------------------|-----------|
| Pentacene | Al ₂ O ₃ | ZnTe | ±15 | 10 | 0.33 | --- | --- | [43] |
| Pentacene | PVP | Au NP | ±90 | 10 | 0.05 | 700 | 1 s | [54] |
| BPE-PTCDI | SiO ₂ /300 nm | PVTT | ±100 | 81 | 0.40 | 100 | >10 s | [45] |
| Pentacene | SiO ₂ /300 nm | P13 | ±120 | 60 | 0.25 | 3000 | 1 s | [55] |
| P3HT | Al ₂ O ₃ | Au-NH ₂ | ±15 | 10.6 | 0.35 | 100 | 1 s | [47] |
| N(PTPMA) ₃ :TIPS-PEN | SiO ₂ /300 nm | PS Brush | -120 to 100 | 55 | 0.25 | 100 | 1 s | [48] |
| F8T2 | PS | Au NPs | ±90 | 30 | 0.16 | --- | 1 s | [49] |
| IPPA-Cl | PS | Doped PS | ±30 | 40.8 | 0.68 | 100 | 10 s | [50] |
| C ₆₀ | Al ₂ O ₃ | Photo chrome | 3 to -10 | 10 | 0.76 | 100 | 10-30 ms | [51] |
| C ₈ -BTBT | PMMA | P(VDF-TrFE) | ±15 | 12 | 0.40 | 100 | 4 ms | [52] |
| C ₈ -BTBT | SiO ₂ /300 nm | (PEA) ₂ PbBr ₄ | ±100 | 180 | 0.9 | >10000 | 0.2 s | This work |